Flow Dynamics Effected by Active Flow Control in an Offset Diffuser

Travis J Burrows,[1] Bojan Vukasinovic,[2] and Ari Glezer[3]
Woodruff School of Mechanical Engineering,
Georgia Institute of Technology, Atlanta, Georgia, 30332-0405

Total pressure distortions at the aerodynamic interface plane (AIP) of an aggressive double-offset diffuser that are induced by the formation of secondary vortices coupled with internal flow separation domains are mitigated by fluidic-based flow control. The presence of the secondary counter-rotating streamwise vortex pairs that form at each diffuser turn induces concentrations of total pressure deficit at the AIP by advecting low-momentum fluid from the wall region into the core flow. The effectiveness of fluidic actuation for suppression of the AIP distortions is demonstrated by implementing actuator arrays at the downstream diffuser turn that leads to over 60% reduction in the average circumferential distortion. Spectral and POD analyses of high-speed, time-resolved total pressure measurements at the AIP indicate that these counter-rotating vortex pairs are unstable exhibiting a frequency band centered about 1 kHz. The actuation alters the spectral content of the pressure fluctuations and leads to their broadband suppression that includes the unstable frequency band of the secondary vortices. The stabilization of the total pressure oscillations is reflected in suppression of not only time-averaged total pressure distortion, but it also reduces a spread of instantaneous distortion about its mean. Consequently, the peak instantaneous flow distortion is reduced by 25%.

Nomenclature

AIP	=	aerodynamic interface plane
C_q	=	jet mass flow rate coefficient
D	=	diffuser AIP diameter
$DC60$	=	engine-face distortion descriptor
$DPCP$	=	SAE circumferential distortion descriptor
$DPCP_{avg}$	=	average SAE circumferential distortion descriptor
f	=	frequency
H	=	diffuser inlet height
L	=	diffuser length
m	=	POD mode
M_{AIP}	=	AIP Mach number
M_t	=	throat Mach number
n	=	number of flow control jets
POD	=	proper orthogonal decomposition
p_{ref}	=	diffuser reference pressure
p_t	=	total pressure
$p_{t,RMS}$	=	RMS of the total pressure fluctuations
$SPOD$	=	spectral proper orthogonal decomposition
W	=	diffuser throat width

[1] Graduate Research Assistant, AIAA Member.
[2] Research Engineer, AIAA Member.
[3] Professor, AIAA Fellow.

I. Introduction

Inlet systems of future fighter aircraft will use embedded engines and more compact, three-dimensionally offset inlet-airframe integration to attain a small spot factor and aerodynamic efficiency. Such inlet systems utilize complex serpentine diffusers that present flow-management challenges, effected by the development of large-scale vortices and boundary-layer separation coupled to throat shocks and aggressive diffuser turns. This secondary-flow phenomenon results in reduced total-pressure recovery and increased flow distortion at the engine face, which can be detrimental to engine operability and performance, but could be mitigated with the implementation of flow-control technology. Passive and active flow control technology have been extensively studied in diffusers, with the goal of improving recovery and distortion at the aerodynamic interface plane (AIP).

The most common passive flow-control device is the vortex generator. Brown et al. [1] tested one and two rows of rectangular vane-type vortex generators, which were designed based on inviscid vortex image theory, in a short, trumpet-shaped Lockheed SST subsonic diffuser, at a diffuser entrance Mach of 0.8. It was found that these vortex generators both increased total pressure recovery and decreased the total pressure distortion. Vakili et al. [2] used vortex generators in a counter-rotating configuration to successfully eliminate flow separation, reduce flow distortion, and increase pressure recovery. Richard and Wendt [3] tested wishbone and tapered-fin style vanes in a diffusing s-duct with an inlet Mach number of 0.6, and found that wishbone-style were ineffective, while tapered-fin-style were effective in generating vortices of opposite sense to the naturally-occurring vortices in the flow, resulting in a slight improvement of pressure recovery, and a halving of the maximum circumferential distortion. Anderson and Gibb [4] numerically and experimentally investigated the usage of corotating rectangular vortex generators in a M2129 inlet s-duct. They were able to numerically predict and experimentally validate an 80% drop in steady and unsteady distortion at an inlet Mach number of 0.8. Jirasek [5] performed a numerical design of experiment (DOE) study on the height, length, spacing, angle, and distance from separation and applied the results to a dual-bend UAV inlet with a fixed AIP Mach number of 0.5. Experimental tests found the optimal vane configuration to reduce DC60 by more than 50%, while leaving pressure recovery almost unchanged. Recently, Tanguy et al. [6] performed stereo PIV at the AIP of an s-duct to investigate the effect of vortex generators on the total pressure distortion and recovery, as well as swirl distortion unsteadiness. They found that vortex generators could reduce DC60 by almost 50% at an inlet Mach number of 0.6, and reduce the swirl-angle fluctuations that were present in the base flow.

Active flow control (AFC) has also been used to improve diffuser performance and mitigate losses with less of a drag penalty that can be associated with static vane vortex generators. One technique used is mass flow insertion using continuous jets; Scribben et al. [7] used microjets in a serpentine diffusing duct, operating at an inlet Mach number of 0.55, to reduce circumferential total pressure distortion by 70%, while improving pressure recovery by 2%, with a C_q of 1%. Anderson et al. [8] numerically investigated microjets' effect in a redesigned M2129 inlet s-duct, and after a DOE optimization study, were able to reduce DC60 below 0.1 with a C_q = 0.5% and M_t = 0.7. Gartner and Amitay [9] utilize a variety of AFC devices, including pulsed jets, sweeping jets, and a blowing slot to improve pressure recovery in a rectangular diffusing duct. The slot was found to not be as effective as the sweeping and pulsed jet arrays, even when used with a higher C_q. Rabe [10] tested microjets in a double-offset diffuser, attached to a bell-mouth, with the bulk flow fluidically driven by a gas-turbine engine, and mass injection driven by bleed from that engine. With a bleed rate of 1% (M_t = 0.55), and at the cruise condition, circumferential distortion was reduced by over 60%. Harrison et al. [11] simulated, and experimentally verified, the favorable superposition of ejector-pump-like suction and blowing for a thick-boundary-layer ingesting serpentine diffuser at M = 0.85 in the freestream. They found that a 50% reduction in DC60 by using a circumferential blowing scheme can be increased up to 75% in the hybrid configuration. In addition to conventional jets, synthetic jets have been tested in internal flows for their effectiveness in improving performance. Amitay et al. [12] investigated separation control in a non-diffusing serpentine duct using an array of synthetic jets, and were able to completely reattach flow up to M = 0.2.

The hybrid control approach, that incorporates both passive and active control, has been studied and proven to be effective for reduction of parasitic drag while maintaining some degree of fail-safe performance, and satisfying the need for adjustable flow control. Owens et al. [13] studied the effect of continuous jets and the combination of vortex generators and jets in a boundary-layer-ingesting (BLI) inlet. The effect of jets alone, at a C_q < 1.5%, able to halve the $DPCP_{avg}$ distortion descriptor, at a freestream Mach number of 0.85. When using vane-type vortex generators in conjunction, they were able to achieve an even better distortion reduction with less than half the C_q. Anderson et al. [14] also used a hybrid approach, using microjets to augment the vortices generated by micro- vanes or ramps, in order to minimize the mass flow injection required. They were able to produce similar improvements to that of only micro-jets with only 10% of the previously required mass flow rate. Gissen et al. [15] utilized a combination of vanes and synthetic jets to achieve a 35% reduction in circumferential distortion in a BLI offset diffuser operating at M_{AIP} = 0.55.

In addition to steady-state analysis, time-resolved, dynamic analysis has been conducted in internal flows. Vaccaro et al. [16] performed a combined experimental and numerical study of tangential jets in an aggressive, rectangular s-duct at a free-stream Mach number of 0.44, and found the actuation to eliminate energy content of distinct unsteady spectral features in the base flow. Recently, Garnier [17] performed spectral analysis on radial and circumferential distortion and total pressure fluctuations at the diffuser AIP to study the unsteady effect of continuous and pulsed blowing at M_{AIP} = 0.2-0.4. After testing different pulsing frequencies, it was found that the unsteady distortion is heavily dependent on it, and that baseline natural frequencies should be avoided as the forcing frequency. Dynamic distortion was found to be reduced the most by continuous blowing, and to a lesser extent in the case of pulsed blowing. In addition, Gil-Prieto et al. [18] performed stereo PIV at the AIP of two serpentine diffusers to analyze unsteady swirl angle and distortion fluctuations to study the effect of varying the duct offset. It was found that duct offset has a large impact in unsteady swirl characteristics, where the higher-offset diffuser exhibited much frequent bulk swirl than the lesser-offset diffuser, which was corroborated by proper orthogonal decomposition (POD) modes of the velocity at the AIP. Lastly, Gissen et al. [19] analyzed some time-dependent aspects of the passive and active flow control elements of the hybrid flow control configuration. They isolated the two dominant modes that induce time-dependent reduction of the flow distortion in the presence of active/hybrid flow control. These modes are associated with the formation of two large-scale vortical structures that are formed by the merging of arrays of small-scale actuation vortices.

The present investigations focus on dynamic analysis of flow management within an aggressive, three-dimensional serpentine diffuser, as shown in Fig. 1. This figure illustrates the two major sources of pressure losses and distortion experienced in the diffuser in the baseline operation, each of them caused by separated domains, at turns in the diffuser geometry. The secondary flow caused by these separated domains results in clear total pressure deficit, which is more severe on the top surface, whose turn is closer to the AIP, and has less time to diffuse, than the bottom surface, where separation occurs at the first turn, further upstream. In addition, domain that is utilized for the flow control integration along the second turn is marked in red. The present investigation utilizes time-resolved total-pressure measurements to characterize the dynamic flow behavior with and without active flow control which mitigates pressure distortion and recovery by an array of fluidic oscillating jets placed upstream of the second-turn separated region.

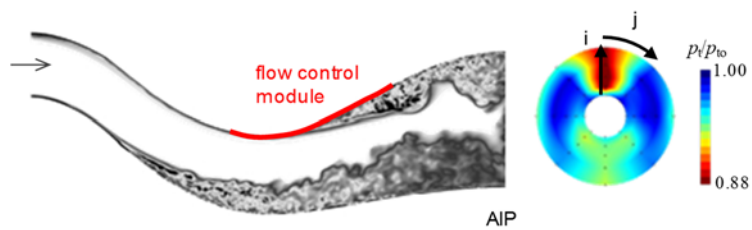

Figure 1. *Illustration of the offset diffuser flow separation and a contour plot of the 40-probe rake measured AIP total pressure distribution.*

II. Experimental Setup and Flow Diagnostics

The present experiments are performed in a small, open-return, pull-down, high-speed subsonic wind tunnel driven by a 150 hp blower in which the temperature of the return air is controlled using a chiller, coupled with an ultra-low pressure drop heat exchanger. An aggressive offset diffuser model is installed in the tunnel such that the tunnel inlet contraction smoothly transitions to the diffuser throat. The diffuser has a *D*-shaped inlet and a round aerodynamic interface plane (AIP) with a diameter, $D = D_{AIP}$ = 0.127 m, and throat Mach number in excess of 0.7 can be realized. The offset between the throat and AIP is $0.4 \cdot D$, length-to-diameter ratio L/D = 3.7, throat width W/D = 1.78, and throat height H/D = 0.48. A flow control module is integrated into diffuser design over the upper downstream surface that triggers the major flow distortion, and can accommodate active flow control elements. In addition, several optical access ports are also integrated into diffuser moldline to be utilized for flow diagnostic techniques.

The main flow diagnostic equipment integrated into the diffuser includes a dynamic pressure rake provided by the Boeing Co. to measure the dynamic total pressure at the AIP according to the SAE industry standard ARP1420b. The rake comprises of 40 miniature high-frequency Kulite pressure transducers that allow for simultaneous sampling frequencies up to 50 kHz, using 40 probes in eight, equiangularly spaced rakes around the circumference of the AIP. In the present experiments, the 40 transducers were sampled simultaneously at 25 kHz over a 5 second interval. This allows for detailed spectral analysis of the total-pressure field. In addition to the dynamic pressures measured by the Kulite transducers, time-averaged, steady state measurements are simultaneously performed at the same locations to assess average pressure magnitudes. The rake pressure ports are referred to using a radial (*i*) and azimuthal (*j*) coordinate system as indicated in Fig. 1, where *i* = 1 at the radially innermost port and 5 at the outermost port, and *j* =

1 indicates the top vertical rake, and each clockwise rake thereafter having an incremented index, where j = 8 for the rake at 315°.

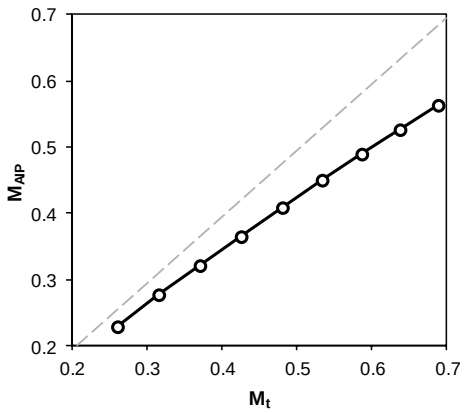

Figure 2. *Variation of the diffuser AIP Mach number with the throat Mach number.*

The AIP total pressure rake is supplemented with a matching ring of eight static pressure ports along the diffuser wall, at the base of each rake leg. In addition, ten and thirteen static pressure ports are distributed along the bottom and top sides of the diffuser wall, respectively. Static and total steady state pressures are measured using a dedicated PSI Netscanner system such that each set of pressure measurements is averaged over sixty-four independent samples, while the mean static and total pressures are based on 100 sets (the uncertainty of the mean pressure is estimated to be less than 1%). The uncertainty of the derived $DPCP_{avg}$ parameter is estimated to be less than 2%. In addition to the static and total pressure measurements, localized visualization of the flow across the control surface is utilized to elucidate the wall flow structure and shed light on the global flow topology.

The two diffuser characteristic Mach numbers relative to the upstream reference pressure p_{ref} were calibrated such that the diffuser Mach number at the throat M_t was measured by the pitot probe centered at the throat cross-sectional area, while the Mach number at the AIP (M_{AIP}) was based on the mean rake AIP total pressure and the corresponding mean wall static pressure, each for a range of flow rates. The resulting calibration curve is shown in Fig. 2, indicating a range of the diffuser flows up to about M_t = 0.69. A nominal operating Mach number is based on the diffuser design requirements, and is set to M_t = 0.64 (M_{AIP} = 0.53).

A spanwise array of equally-spaced (6.3 mm apart) fluidic oscillating jets, with number of jets varying from 3 to 13 (as the array of Burrows et al., [20]), is located upstream of separation (as determined by surface oil visualization) in the second turn (Fig. 3). Each jet orifice measures 1.5 × 2 mm, with an operating frequency between f = 7 – 9 kHz over a range of flow rates. The flow control jets are oriented relative to the streamwise direction such that half the array on each side of the spanwise centerline is skewed towards the sidewall of the duct. The jet mass flow rate coefficient C_q is considered the flow control parameter and it is defined as a ratio between the jet and diffuser mass flow rates, and in the present investigations it is less than 1% in all controlled cases. Further details about the flow control jets were presented in Burrows et al. [20].

To elucidate coherent flow structures, modal decomposition techniques are often used on the time-resolved flow properties. Proper orthogonal decomposition (POD) is used in the present work to identify coherent structures in a flow field. Space-only POD, which decomposes data into a set of spatially orthogonal modes (eigenvectors) with corresponding energy levels (eigenvalues) and time coefficients, is referred to as POD. Another form of POD is used, called spectral proper orthogonal decomposition (SPOD), which refers to the method discussed by Towne et al. [21]. SPOD, in contrast to POD, decomposes data into modes that evolve coherently in space and time [21]. Therefore, SPOD decomposes data into sets of modes for each frequency, the first of each set being the most significant mode of the corresponding frequency. This is a powerful tool, allowing for the visualization of spatial modes that correspond to flow unsteadiness at specific, known frequencies. The relationship between the two POD techniques will be discussed in the present data analysis.

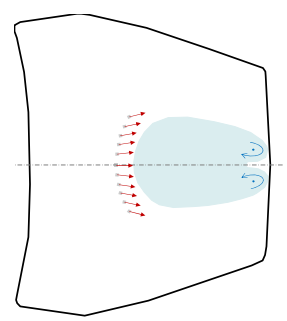

Figure 3. *Schematic of the fluidic oscillating jets integrated into the flow control module.*

III. The Base Flow

The steady-state base flow was characterized by Burrows et al. [20], who elucidated structural details using surface oil flow visualization, at throat Mach number of 0.64. Two separated domains were found, each triggering a pair of counter-rotating streamwise vortices. The first domain is indicated by the onset of separation in the corners of the diffuser D-shaped throat, as shown in Fig. 4a. At the throat, the flow is centrally attached, indicated by the oil streaks created by high-momentum, near-surface fluid, but as the flow evolves, the separation in the corners grows until connecting across the full span on the bottom surface, indicated by the regions of oil without streaks. The presence of counter-rotating, circulating flow at the spanwise edges is evident, and marked by the arrows. This separation pattern indicates highly three-dimensional nature of the flow along the first bend, that leads to the upwelling of low-

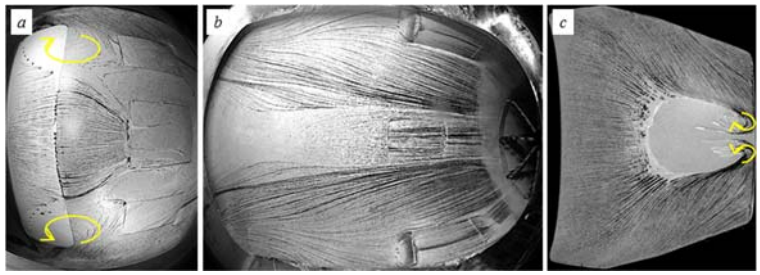

Figure 4. *Surface oil-flow visualization on the duct surface at M_t = 0.64 for the incipient (a) and full (b) upstream and downstream (c) flow separation. Flow is left to right.*

momentum fluid from the bottom surface towards the center of the AIP. The downstream extent of the first-turn streamwise vortex pair is seen in the extended oil-visualization view shown in Fig. 4b, where the two vortical imprints are clearly seen on either side of the central plane of symmetry. The signature of these vortices, in the form of total-pressure deficit, is also seen in the bottom portion of the AIP in Fig. 5a. The second separation domain found along the upper surface after the second bend (Fig. 4c), where the compact separation bubble symmetrically spans the diffuser centerline. Oil streaks, or lack thereof, clearly indicate the separated region, but also show that it is bound by strong streamwise vortices. Of the two pairs, these vortices produce the dominant flow distortion and pressure deficit at the AIP, indicated by the intense low-pressure region in the top center of the AIP contour in Fig. 5a, that is created by lower-momentum fluid being swept up from the surface into the central region by the vortices.

In addition to steady-state measurements, the flow at the AIP was characterized using dynamic, time-resolved measurements of the AIP total pressures. This yields important topological assessment of the dynamics and intensity of coherent motions that are associated with the presence of the streamwise vertical structures in the base and controlled flows. A summary of the dynamic analysis of the base flow is shown in Fig. 5. For reference, Fig. 5a shows the time-averaged AIP total pressure, which contains the signatures of the two pairs of streamwise vortices, coupled to separation domains at the first (bottom) and second (top) diffuser turns. Two AIP pressure transducers, marked in each separation domain ("A" and "B" in Fig. 5a), are chosen for further analysis, as representations of the two domains. A family of spectra of total pressure fluctuations for transducer "A" is shown in Fig. 5b for several diffuser Mach numbers. These spectra exhibit some spectral peaks within a relatively flat range below 1 kHz, followed by a sharp drop off at a slope closely following -5/3, and demonstrate that the energy levels increase with the Mach number. A similar group of spectra for transducer "B" is shown in Fig. 5c. However, compared to the fairly featureless spectra of transducer "A", these spectra exhibit distinct peaks at about 1 kHz where the frequency of these peaks weakly increases with the diffuser Mach number (the other transducers in this domain also exhibit similar spectral peaks). Considering the earlier discussion of the findings about the relationship between the topology of the pressure deficit and the structure of the counter-rotating streamwise vortices that are coupled to separation in the diffuser turns, it is argued that this frequency is associated with an inherent instability of these vortex pairs. Another important observation in the time-resolved total pressure contours is that the time-averaged lower-wall total pressure deficit results from the highly unsteady motion of the vortices that are triggered farther upstream and therefore may be less coherent (in a time-averaged sense). In fact, instantaneous pressure contours in the lower half of the AIP intermittently exhibit two disparate nodes of the total pressure deficit, as shown in Fig. 5d that are ostensibly associated with two distinct streamwise vortices along the lower wall. The pressure data indicate that these vortices meander such that their cores are closer or farther apart by the time they reach the AIP. This unsteadiness is manifested by an absence of a sharp peak in the spectra of Fig. 5b.

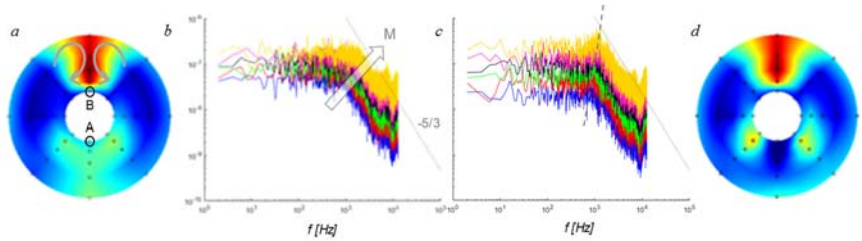

Figure 5. *Contour plots of the time-averaged (a) and instantaneous (d) AIP total pressure, and the power spectra of the total pressure fluctuations at transducer A (b) and B (c), with the varying diffuser Mach number.*

IV. Flow Control Effects

The steady-state effect of flow control actuation is illustrated by surface oil flow visualization (Fig. 6a-d) and total pressure AIP contours (Fig. 6e-h) by Burrows et al. [20], in addition to present total-pressure RMS fluctuation contours shown in Fig. 6i-l. Baseline flow (Fig. 6a), indicates the second-turn separation domain and signatures of the coupled streamwise vortices that are present in the natural, uncontrolled flow, Fig. 6b-d show the resulting surface oil flow

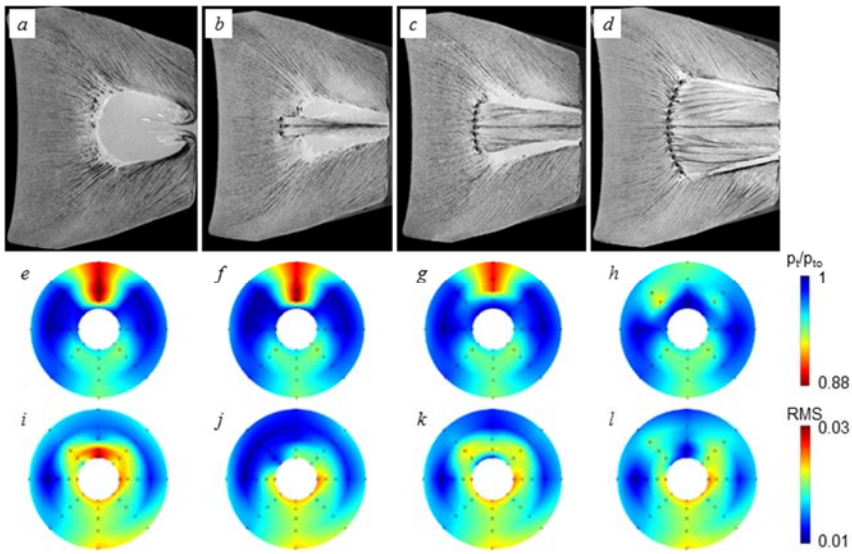

Figure 6. *Surface oil-flow visualization over the downstream flow control insert (a-d), and contour plots of the AIP total pressure time-averaged (e-h) and RMS fluctuations (i-l) with flow control parameter $C_q/n = 3.2\times10^{-4}$ and varying number of active jets $n = 0$ (a,e,i), 3 (b,f,j), 7 (c,g,k), and 13 (d,h,l) at $M_t = 0.64$.*

visualizations in the same region for the cases of n = 3,7, and 13 flow control jets, respectively, holding C_q/n constant at 3.2×10^{-4}, and the throat Mach number of 0.64. When just three jets are utilized, a major topological change is apparent on the diffuser second-turn surface, where these three jets pierce the separation bubble, causing the flow to attach at the centerline, bifurcating the separated region into two smaller domains. Despite the obvious change in the surface topology, effect on the steady-state AIP total pressure is more difficult to discern. It is apparent that this low-n array slightly lowers the intensity of the low momentum, high pressure deficit region. The n = 7 array has greater effect on both the surface topology and total pressure. The region that was previously separated in the baseline is almost fully attached, with strips of separation on either side. The effect at the AIP is more evident in this case, with the upper low-momentum zone being both decreased on intensity and size, effecting a 22% decrease in $DPCP_{avg}$. The most prominent change is seen in the case of 13 jets, where the flow is fully attached after the second turn. Coherent barriers form on either side of the attached region, which are imprints of the streamwise vorticity, are displaced laterally outward from baseline, separating the two original vortices, which are each paired with vorticity generated by the canted jet array, causing two nodes to appear in the total pressure at the AIP. This results in a $DPCP_{avg}$ reduction of 57% at C_q = 0.44%.

Additional insight in the flow control effect on the flow is gained by analysis of the AIP contours of the total pressure RMS fluctuations (Fig. 6i-l). It is seen that high RMS levels of the base flow (Fig. 6i) are distributed about the upper hub domain, and are attributed to the inherent instability of the upper pair of streamwise vortices. Aside from the hub region, the RMS fluctuations in the base flow are somewhat elevated along the lower surface, which is associated with the dynamics of the second vortex pair originating from the diffuser throat. When the flow control utilizes only the three jet (Fig. 6j), the upper hub RMS fluctuations become fully suppressed, implying that one of the effects of n = 3 actuation is the stabilization of the upper vortex pair. There is an increase in RMS fluctuations, relative to the n = 3 case, when the flow control is effected by seven jets. Nonetheless, the focused high-intensity RMS levels of the base flow become diffused over the extended upper hub area under this flow control case. This trend in redistribution of the high levels of the total pressure RMS fluctuations evolves further as the flow control is expanded to n = 13 case (Fig. 6l). The elevated RMS levels off the hub area appear more as the two nodal structures, separated by the low-RMS central zone. These two nodes align with the two signatures of the interacting base and control vortices [20]. It should be noted that the best flow control case in terms of pressure recovery and distortion (n = 13) does not exhibit the lowest RMS fluctuations (which is n = 3), owing to the interaction dynamics between the follow control and natural streamwise vortices that mitigates distortion and assists in recovery.

Another interesting observation is emphasized in Fig. 7, where the three characteristic flow control cases are compared, having the n = 3, 7, and 13 central active jets. Both the time-averaged and RMS fluctuations of the AIP total pressure are shown for each of these control cases, for the flow control C_q scaled by the number of jets, n. Figure 7a shows

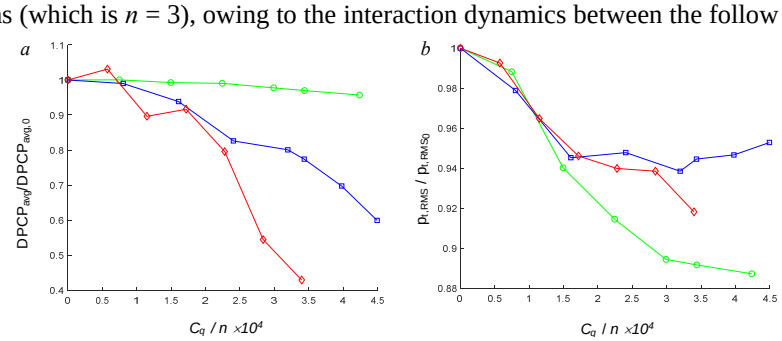

Figure 7. *Circumferential distortion parameter $DPCP_{avg}/DPCP_{avg,0}$ (a), and total pressure RMS / RMS_0 for n = 3, 7, 13.*

the steady-state $DPCP_{avg}$ scaled by the steady-state $DPCP_{avg}$ without actuation ($C_q = 0$), and Fig. 7b presents the total-pressure RMS fluctuations scaled also by the baseline, all of which are at $M_{AIP} = 0.49$. As seen in Fig. 7a, actuation by only three central jets does not significantly affect the flow distortion. However, the corresponding time resolved measurements (Fig. 7b) indicate that this control does reduce the flow unsteadiness, which, combined with virtually no effect of the distortion, suggests that this particular flow control approach actually stabilizes the vortex pair responsible for the total pressure deficit along the upper diffuser surface. This stabilization is also seen in the contour plot of Fig. 6j, where low levels of the total pressure RMS are expanded outward from the upper diffuser surface when compared to the base flow (Fig. 6i). The other two flow control approaches, which are both successful in reduction of the total pressure distortion in the average sense, as seen in Figure 7a, are found to decrease the RMS levels at lowest level of C_q (Fig. 7b), and approaching asymptotic levels afterwards, with a further increase in C_q. This net effect can be explained by the competing effects of the reduced RMS levels due to the suppressed flow separation along the upper surface, and the weakening of the corresponding vortex pair, while at the same time exhibiting nodal increases in the RMS levels about the interacting flow and controlled vortices. In a sense, the total pressure distortion suppression in the average sense is achieved by the disruption and mixing of the flow-dominant streamwise vortex pair, by enhancement their interaction and inevitably increased localized unsteadiness.

V. Flow Dynamics

Another insight into the time-resolved flow distortion is attained by calculation of the circumferential face-averaged distortion parameter $DPCP_{avg}(t)$ for each realization of the 40-probe rake measurements. Fig. 8 presents the time-resolved analysis of the $DPCP_{avg}(t)$ distortion parameter for the base flow and the flow controlled by n = 3, 7, and 13 active jets. Probability density functions of the time-resolved $DPCP_{avg}$ are shown in Fig. 8a, indicating a clear shift towards the lower distortion levels, in addition to a decrease in standard deviation, with an increase in the number of active jets. These distributions also indicate a rather wide range of distortion, symmetrically distributed about the most probable levels of distortion. For instance, although the time-averaged $DPCP_{avg}$ of the base flow is estimated to be about 0.038, its distribution indicates peak values up to about 0.076. As the most effective flow control approach is applied (n = 13), not only the most probable distortion levels are significantly reduced, but the surge levels of $DPCP_{avg}$ are also reduced by about 25%. Although it was already shown that the corresponding reduction in $DPCP_{avg}$ of the steady-state flow is over 50%, the pdfs in Fig. 8a indicate that the most expected levels of the time-resolved distortion decrease by about 25%. This discrepancy is attributed to the smearing effect of the highly unsteady vortices in the time-averaged total pressure distributions, whose dynamics becomes resolved in the high-frequency measurements. Still, it should be noted that the high-frequency swings in the total pressure deficits about the AIP would not necessarily impact the engine performance. Lastly, the dominant frequency measured about the upper wall vortices of about 1 kHz (Fig. 5c) clearly propagates into the distortion parameter dynamics, as seen in all the spectra of the $DPCP_{avg}(t)$ considered in Fig. 8a that are shown in Fig. 8b. It should be also noted that, in spite of the peak frequency presence in all of the cases, there is a slight shift in its value with different actuation approaches. Furthermore, the energy level of the dominant frequency somewhat decreases with an increase in the number of active jets n.

In addition to instantaneous analysis of the face-averaged $DPCP_{avg}$, each per-ring circumferential distortion, $DPCP(i)$, is assessed as well. The face-averaged descriptor gives an indication of the overall distortion, but individual ring distortions can give a better idea of the radial contribution to $DPCP_{avg}$. These individual $DPCP$ distributions are shown in Fig. 9. On the left, Fig. 9a and 9f show the spectra and *pdf* of the $DPCP$ at the hub, or innermost ring of the AIP (i = 1), and the rightmost plots, Fig. 9e and 9j, show that of the tip, which is the outermost ring of the AIP (i = 5). It is apparent that the innermost ring, closest to the core diffuser flow, is the least affected by flow control actuation, at least in terms of pressure distortion. There is minimal difference between cases in both the magnitudes of fluctuation in the spectra and the distribution of values of $DPCP$, indicated in the *pdf*. This region is the furthest from the region where flow control is effected, along the diffuser surface. Low momentum fluid at the AIP, in both the

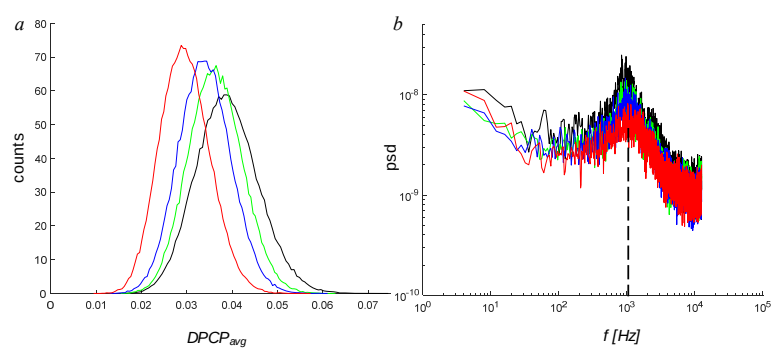

Figure 8. *Probability density function of a time-resolved $DPCP_{avg}$ parameter (a) and its corresponding power spectra (b) for n = 0, 3, 7, and 13 active jets.*

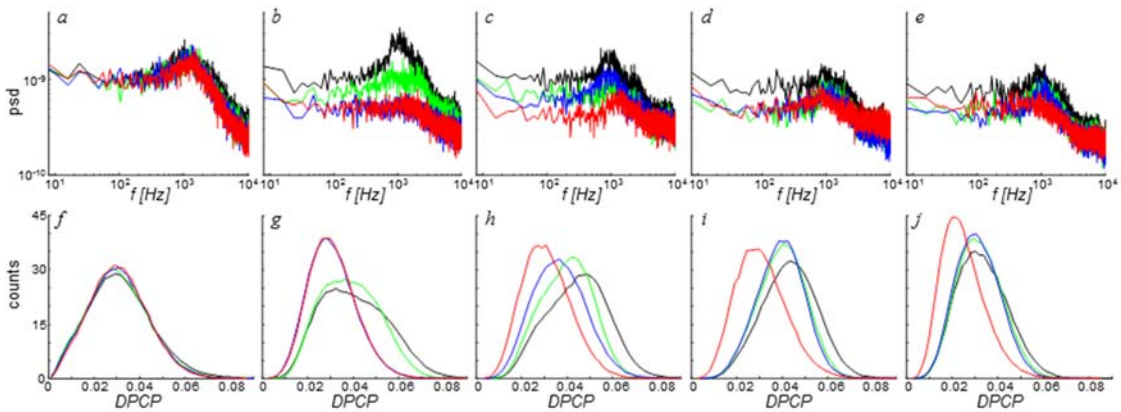

Figure 9. *Probability density function of a time-resolved DPCP for each ring i = 1-5 (a-e) and its corresponding power spectra (f-j) for n = 0, 3, 7, and 13 active jets.*

base and control cases, doesn't get elevated this far radially, away from the surface. The next ring away from the bulk flow, $i = 2$, however, gets affected by actuation. The magnitude of the distortion in this ring is widely and quite evenly distributed, indicated by the fairly flat *pdf* in Fig. 9g. The base spectra has a peak at 1 kHz, which becomes suppressed even with $n = 3$. When $n = 7$ or 13, the spectra is rendered featureless, and the distribution of *DPCP* is dramatically improved, with a much lower most probable distortion value, and a much narrower distribution. Ring 3 has the most consistent improvement with the increasing n – with each increase in n, the power spectral density is decreased, particularly at $f = 1$ kHz and below, and the standard deviation of *DPCP* is decreased. Rings 4 and 5 also have the spectral peak at 1 kHz, though less prominent than rings 2 and 3. Effect on the fluctuations and distribution of *DPCP* is not as dramatic in these outermost regions. The effect of increase in n in ring 4 seems to be the flattening the spectra, by decreasing the magnitude in the 1 kHz range, and increasing the *psd* in the 10 kHz range, which is attributed to the flow control jets operating frequency range. In both ring 4 and 5, $n = 3$ or 7 have a similar effect on the *DPCP* distribution, while an increase of n to 13 results in a distinctly larger reduction in the *DPCP* distribution magnitudes.

Spatially-coherent structures associated with the time-resolved measurements of the AIP total pressures are identified using POD modes of the total pressure fluctuations, and shown in Fig. 10. The first five modes for the base flow, and $n = 3$, 7, and 13 are shown. In the base flow, the first, dominant mode corresponds to the region identified with the highest RMS fluctuations (Fig. 6i). The following modes still have a comparable energy fractions: modes 2 and 5 are also related to the upper-surface unsteadiness, while the third and fourth modes appear related to the lower surface pressure fluctuations. When examining the first POD modes of the actuated cases ($n > 0$), it is noteworthy that the dominant mode of all the controlled cases does not have the same structure as its base flow counterpart. Instead, its structure resembles the base flow second mode, indicating that the flow control eliminates the base flow dynamics that gives a rise of its most dominant dynamic structure. This is most apparent in the case of $n = 3$, where the steady-state total pressure pattern is visually the most similar to the baseline. Not only does the first mode of $n = 3$ resemble the first mode of $n = 0$, but modes 2 and 3 of $n = 3$ also are structurally very similar to modes 3 and 4 of $n = 0$. Therefore, the effect of the flow control by $n = 3$ is essentially manifested solely in eliminating the dominant instability of the upper-surface vortex pair that is represented by the first

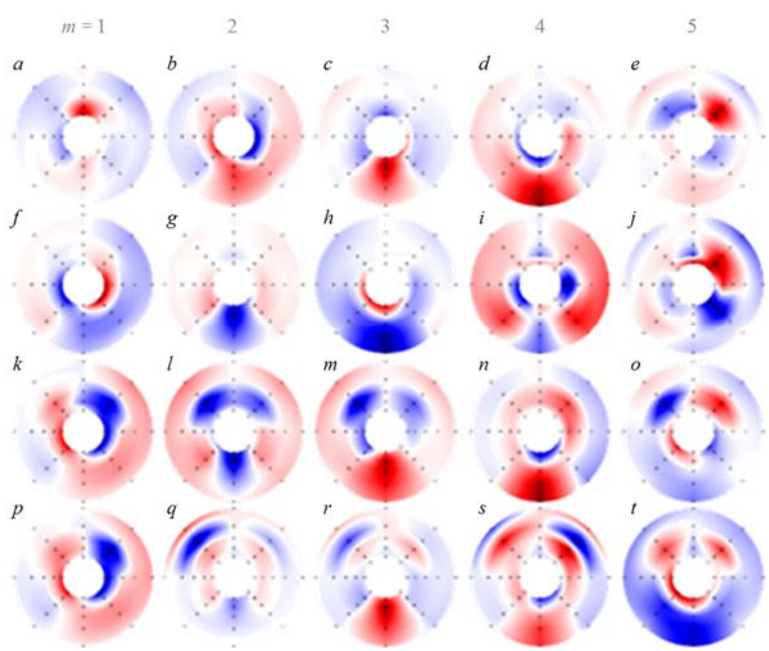

Figure 10. *POD modes m = 1-5 (columns) for the active number of jets n = 0 (a-e), 3 (f-j), 7 (k-o), and 13 (p-t).*

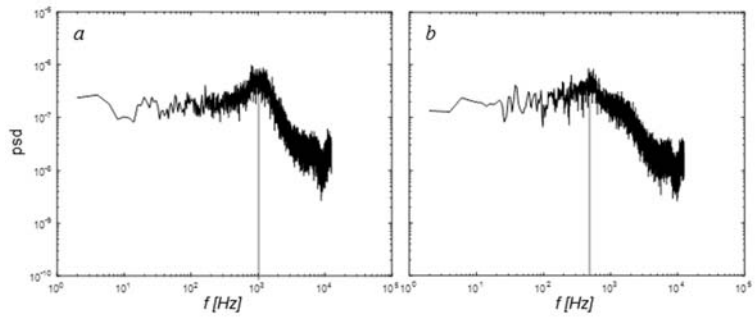

Figure 11. *Power spectra of the base flow time coefficients that correspond to the POD modes m = 1 (a), and 5 (b).*

base POD mode. This is in accord with the RMS pressure fluctuations previously discussed in Fig. 6 – RMS of n = 3 is structurally similar to RMS of n = 0, except for the high intensity region in the top of the AIP hub. The cases of n > 3 also eliminate this first mode, but have a more profound effect of other dynamics, as represented by dissimilar modes past mode 2, that is ultimately also represented in the significantly altered time-averaged total pressure contours (Fig. 6). Another observation is that actuation with any n does not significantly modify the modal energy distribution at the AIP within each of these cases, although there is a slight increase in energy in the first mode with every increase in n. Lastly, it is noted that when examining the time coefficients associated with the POD modes, in the base flow, two of the first five modes exhibit characteristic peaks in the power spectra. These modes are modes one and five (Fig. 11a and 11b), where mode one contains a peak at 1 kHz, while mode five contains a peak at about 500 Hz. Since POD modes are not related to a particular flow frequency (time scale), each mode typically represents phenomena at many different time scales or frequencies [21]. Therefore, the spectral peaks shown in Fig. 11 indicate only that a prevailing contribution of these modes, one and five, are from the frequency bands at 1,000 and 500 Hz, respectively. To extract flow phenomena associated with relevant frequencies, SPOD is used, the modes of which depend on both space and time scales. The SPOD algorithm by Towne et al. [21] is used, with 249 blocks of 1,000 snapshots each, and 50% overlap. This decomposition is able to identify more optimal modes, which better capture significant energy fractions of the flow. This is demonstrated by integrating the energy spectra of each mode over frequency, yielding the total energy of each mode across all frequencies, comparable to relative energy values in space-only POD. Fifty percent of the total energy is contained in the first 7 SPOD modes, in contrast to 12 modes needed in the space-only POD.

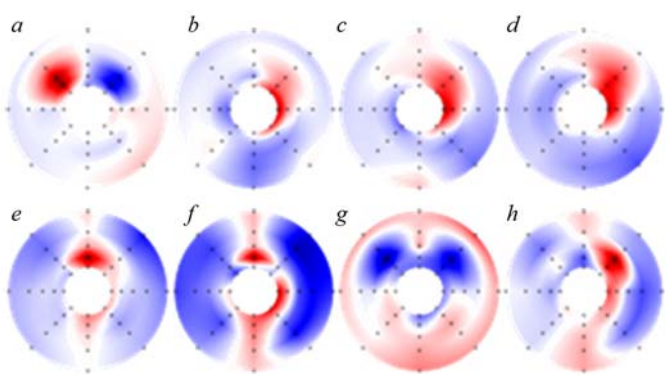

Figure 12. *First SPOD mode for the frequencies 475 (a-d), and 1,000 Hz (e-h), for n = 0 (a,e), 3 (b,f), 7 (c,g), and 13 (d,h).*

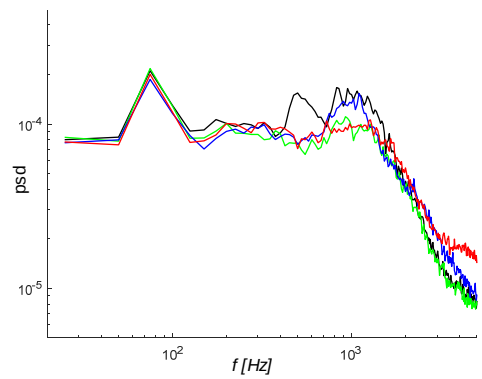

Figure 13. *First SPOD energy spectra, integrated across all frequencies for n = 0, 3, 7, and 13 active jets.*

Figure 12 shows the first mode for n = 0, 3, 7, and 13 for the two dominant frequencies in the base flow first mode SPOD energy spectra (cf. Fig. 13). A clear connection between these modes and the POD modes discussed in Fig. 10 is noted. The first mode at 1 kHz in Fig. 12 has a similar structure to that of the first baseline POD mode, which can be expected due to the known 1 kHz peak of the time coefficient spectra of the POD mode, as shown in Fig. 11a. The same connection can be drawn between the first base flow SPOD mode at 475 Hz. This mode has a similar structure to the fifth baseline POD mode, which has a time-coefficient spectral peak around 500 Hz.

Analysis of the flow control effect on these spatio-temporal modes is presented in Fig. 13 in terms of the energy spectra of the most dominant SPOD modes for the base and the flow controlled by n = 3, 7, and 13 jets. When examining the energy spectra for the first SPOD mode in Fig. 13, it is observed that the baseline peak at ~475 Hz is eliminated in all the controlled flow cases (n > 0). The corresponding first SPOD modes reflect a structural change associated with this frequency – the two-node structure of the first baseline 475 Hz SPOD mode is no longer present at this frequency in the first modes of all the actuated cases, indicating that the unsteadiness in the base flow associated with this frequency is bypassed when actuation by any number of the presented jets is used. Upon examination of the first 1 kHz SPOD mode for each of the four cases shown in Fig. 13, it is apparent that the case of n = 3 contains a

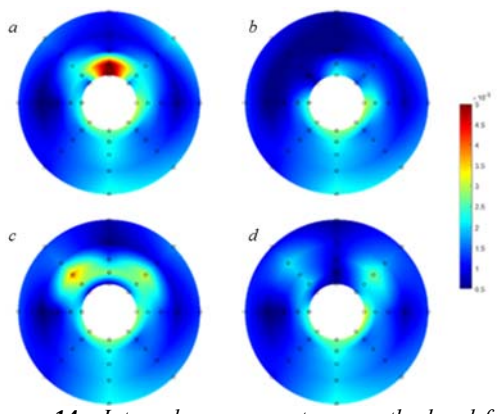

Figure 14. *Integral power spectra over the band f = 900-1,100 Hz for n = 0 (a), 3 (b), 7 (c), and 13 (d).*

similar structure to that of the baseline mode. However, as the spectral peak at this frequency is suppressed for this flow control case, relative to the base flow, it is argued that in spite of this spatial structure being present in the controlled flow, its dynamics still becomes suppressed. Interestingly, the first mode power spectra for n = 7 indicates a peak at 1 kHz that n = 3 and n = 13 cases do not feature, suggesting that in this case, there are still significant flow fluctuations at this frequency, in spite of the coherent structure being completely different than that of the base flow, and somewhat resembling the corresponding second and third POD modes, which also have time-coefficient spectral peaks at this frequency. This observation further relates the POD and SPOD analysis, as each POD mode can be, in principle, consisted of multiple SPOD modes, as also noted by Towne et al. [21]. Peaks in the POD-coefficients spectra indicate which frequency is most associated with the corresponding POD modes, but SPOD extracts both the spatial and temporal information.

Another indication of the flow domains associated with the dominant frequency are sought by integration of the power spectra about the most prominent frequency band about 1 kHz. Figure 14 shows the contour plots of this integral measure across AIP for each of the four cases studied. The base flow (Fig. 14a) contains high energy levels of this band at the top of the hub, which is in agreement with the peak RMS fluctuations seen in Fig. 6i. This flow feature is captured in both POD and SPOD, and is attributed to the unsteady interaction of the pair of counter-rotating vortices along the top diffuser surface. When the flow control n = 3 is utilized, this energy band becomes greatly suppressed about the hub (Fig. 14b), and no other regions of fluctuation within this band appear over the AIP. This is also in agreement with an earlier observation that, when n = 3, the flow POD structure (Fig. 11) was quite similar to the base flow, except lacking the first base flow POD mode. When n = 7 (Fig. 14c), the high energy band of the base flow disappears; however, a lesser intensity, larger area of this amplified band emerges around the original domain, indicating a spreading effect. This spreading has a somewhat similar shape to the first 1 kHz SPOD mode, and is also in accord to the SPOD spectra (Fig. 13), indicating that the fluctuations increase from n = 3 to n = 7. Lastly, when n = 13 (Fig. 14d), regions of moderate energy level of the examined band appear in the regions that correspond to the low time-averaged total pressure (cf. Fig. 6h).

As the flow control case n = 13 is considered to be a locally-optimal case (see also Ref. [20]), it is characterized in more detail by varying the diffuser Mach number. RMS total pressure fluctuations relative to steady-state total pressure, and the peak AIP face-averaged distortion are shown in Fig. 15 a and b, respectively, for the throat Mach numbers ranging from 0.41 to 0.53. Regardless of M, an increase in C_q decreases the average AIP fluctuations. The peak $DPCP_{avg}$ in the time-series (Fig. 15b) shows a similar trend, while both the RMS and peak distortion in the base flow increase with M, as it can be expected. Increasing the flow control parameter C_q results in a larger effect of the suppression of the peak distortion, compared to the effect on the RMS fluctuations. For M_t = 0.53 and highest C_q = 0.44%, the peak distortion becomes decreased below that of M_t = 0.45 without actuation (C_q = 0). Fig. 15c shows the time-averaged $DPCP_{avg}$, scaled by the value at baseline, or at C_q = 0. The scaled distributions collapse onto the same curve, indicating that the relative decrease of steady-state distortion is independent of M (within the tested range), and that depends only on the flow control parameter C_q.

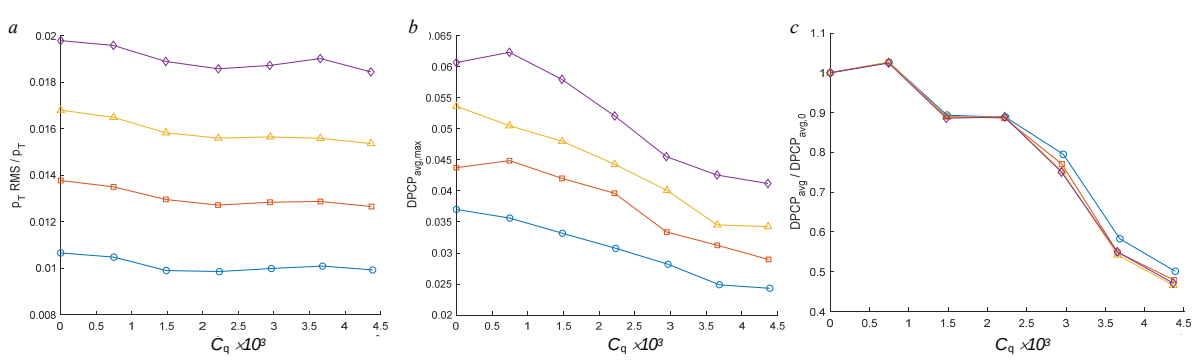

Figure 15. *RMS fluctuations of p_t (a), maximum instantaneous $DPCP_{avg}$ (b), and steady-state $DPCP_{avg}$ / $DPCP_{avg,0}$ (c) at M_t = 0.41, 0.45, 0.49, 0.53, and n = 13.*

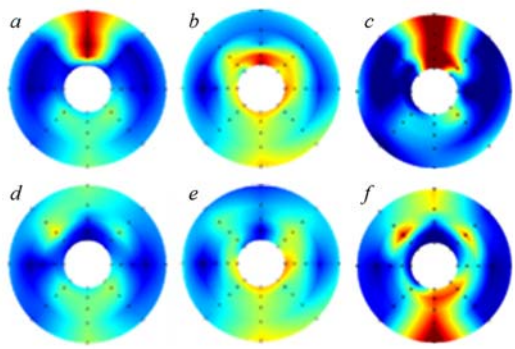

Figure 16. *AIP mean (a,d) total pressure and RMS fluctuations (b,e), and the instant of maximum $DPCP_{avg}$ (c,f) for cases n = 0 (a-c) and 13 (d-f).*

The resulting effect of the optimal flow control case (n = 13) is emphasized relative to the base flow in Fig. 16, where the mean, RMS, and the peak-distortion total pressure contour plots are shown. Effectiveness of the flow control is brought about by bifurcation of the base-flow streamwise vortex pair along the upper surface by the small-scale streamwise vorticity imposed by the fluidic oscillating jets, resulting in the AIP signatures of two lesser-strength nodes of the total pressure deficit in the controlled flow (Fig. 16d), compared to a single domain of strong pressure deficit in the base flow (Fig. 16a). In addition, regions of high RMS about the hub (Fig. 16b) are redistributed to the regions of interaction of the control and the base vortices, as seen in Fig. 16e. Vortices in each streamwise-vortex pair in the actuated flow. Finally, a snapshot of the total pressure distribution at the peak distortion shows a rather dramatic suppression of the total pressure deficit along the upper (controlled) flow domain (Fig. 16f). Interestingly, successful suppression on that side intensifies peak total pressure deficit on the opposite (uncontrolled) surface. Overall, there is a significant suppression in the peak AIP distortion for the controlled flow, in addition to the suppressed distortion in the time-averaged sense.

To further examine a local effect of the optimized flow control across the upper AIP domain, Fig. 17 compares the spectral content for a selection of the 15 probes in the top angular segment of -45°, 0°, and 45°, symmetric about the vertical plane of symmetry. As seen in the power spectral density of the total pressure fluctuations across this segment, the primary effect of the flow control is manifested in the broadband suppression of energy across the frequencies. To emphasize this dominant effect, power spectra of the base and controlled flows at (1,1) are shown in Fig. 17c. Along with this general attenuation in the pressure fluctuation energy, there are additional, more localized effects. For instance, spectral peaks at 500 Hz (particularly dominant in ports (2,8), (3,8), and the symmetric counterparts (2,2) and (3,2) are bypassed in the controlled flow, and instead, in the n = 13 case, lesser-power peaks exist at 1 kHz. It is interesting that this location coincides with the nodal structure of the SPOD dominant mode at 1,000 Hz of the controlled flow, while the same position corresponded to the dominant SPOD mode of the base flow at 475 Hz (cf. Fig. 12 and 13). This shift in the characteristic frequency is also emphasized in direct comparison between the uncontrolled and controlled spectra at (2,8), which are shown in Fig. 17f. At a couple of locations, there is an increase in the total pressure fluctuations in the controlled flow, as seen at (4,8) and (4,2). These two ports are symmetric across the centerplane, and are in the regions of reduced total steady-state AIP pressure (Fig. 16d), i.e., they directly characterize two regions of the forced interaction between the control and natural streamwise vortices on either side

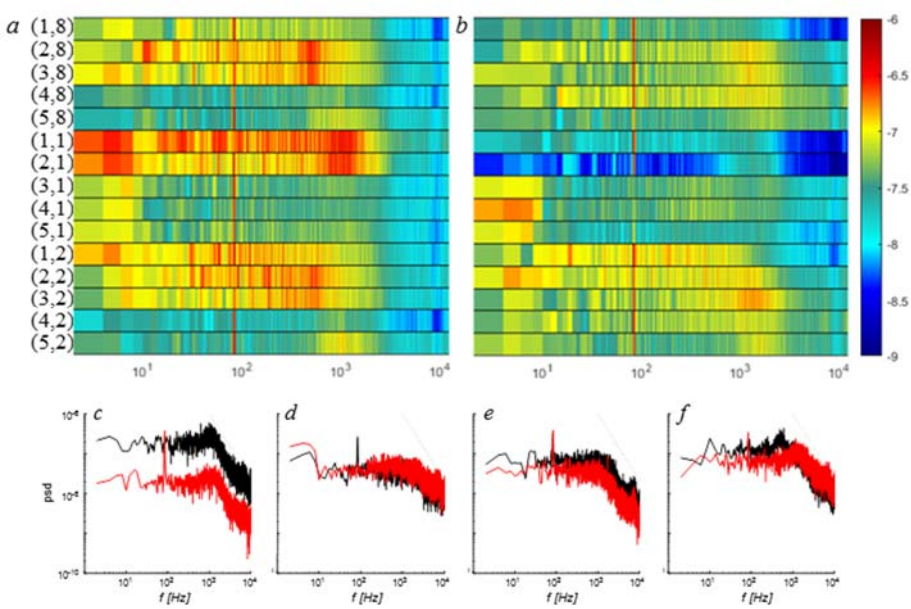

Figure 17. *Contour plots of total pressure power spectra for the base (a) and the flow controlled by n = 13 (b) jets, and power spectra of ports (1,1) (c), (4,1) (d), (1,8) (e), and (2,8) (f), for the base (—) and controlled (—) flows.*

of the central plane of symmetry. Lastly, there are few ports that do not exhibit significant difference between the controlled and uncontrolled flow, which is illustrated in Fig. 17d for the port (4,1).

VI. Conclusions

The present experimental investigation has focused on mitigation of total pressure distortions within an aggressive double-offset diffuser that are induced by the formation of secondary vortices within the core flow. These streamwise counter-rotating vortex pairs are engendered by spanwise concentrations of trapped streamwise vorticity that form in the outboard segments of the vorticity layer bounding separated flow domains within on the concave surfaces of each diffuser turn. These vortices effect total-pressure distortion by advecting low-momentum fluid from the wall region into the core flow. Active flow control using arrays of surface-mounted fluidic oscillators targets the coupling between the streamwise vortices and the trapped vorticity within internal flow separation domains by using surface-integrated fluidic actuation. It is shown that the manipulation of these trapped vorticity concentrations can lead to significant diminution of the distortion. Time-dependent and –averaged characteristics of the diffuser flow in the absence and presence of flow control were investigated at diffuser throat Mach numbers up to M_t = 0.64 using an AIP dynamic total-pressure rake, distributions of surface pressure, and surface oil-flow visualization.

Fluidic-oscillating jets skewed towards the diffusers side wall on each half of the span (C_q = 0.44%) are used to induce predomoinantly single-sign streamwise vorticity of opposite sense to that of the adjacent outboard streamwise vorticity concentration formed by the separated domain. The presence of the jet-induced streamwise vorticity diminishes the separation and alters the rollup of the base flow counter-rotating vortex pair resulting in significant spanwise displacement and weakening and thereby reducing the AIP distortion in excess of 60%.

Further insight into dynamics and intensity of coherent motions that are associated with the presence of the streamwise vortical structures in the base and controlled flows is gained by time-resolved measurements of the AIP total pressure distribution. These measurements, which were acquired at 25 kHz revealed that the total pressure deficit at the AIP that are brought about by the presence of streamwise vortex pairs are unstable and meander laterally within the diffuser's core flow with a characteristic frequency band centered about 1 kHz. Furthermore, spectral and SPOD analysis of the time-dependent measurements provided a link between the coupled spatio-temporal changes in the controlled flow relative to the base diffuser flow. The present measurements show that active flow control has a profound effect on the topology and stability of these vortices and suppresses the dominant natural spectral components of the base flow. Along with the time-averaged descriptors of the AIP total pressure distribution the attenuation of the *instantaneous* variations in the circumferential distortion exceeds 25%.

Acknowledgements

This work has been supported by ONR, monitored by Dr. Steven Martens.

References

[1] Brown, A. C., Nawrocki, H. F., and Paley, P. N. "Subsonic diffusers designed integrally with vortex generators," *Journal of Aircraft* Vol. 5, No. 3, 1968, pp. 221-229.
doi: 10.2514/3.43931

[2] Vakili, A., Wu., J., Liver, P., and Bhat, M. "Flow control in a diffusing S-Duct," *Shear Flow Control Conference*. American Institute of Aeronautics and Astronautics, 1985.

[3] Reichert, B. A., and Wendt, B. J. "Improving curved subsonic diffuser performance with vortex generators," *AIAA Journal* Vol. 34, No. 1, 1996, pp. 65-72.
doi: 10.2514/3.13022

[4] Anderson, B. H., and Gibb, J. "Vortex-Generator Installation Studies on Steady-State and Dynamic Distortion," *Journal of Aircraft* Vol. 35, No. 4, 1998, pp. 513-520.
doi: 10.2514/2.2340

[5] Jirasek, A. "Design of Vortex Generator Flow Control in Inlets," *Journal of Aircraft* Vol. 43, No. 6, 2006, pp. 1886-1892.
doi: 10.2514/1.21364

[6] Tanguy, G., MacManus, D. G., Zachos, P., Gil-Prieto, D., and Garnier, E. "Passive Flow Control Study in an S-Duct Using Stereo Particle Image Velocimetry," *AIAA Journal* Vol. 55, No. 6, 2017, pp. 1862-1877.
doi: 10.2514/1.J055354

[7] Scribben, A., Ng, W., and Burdisso, R. "Effectiveness of a Serpentine Inlet Duct Flow Control Technique at Design and Off- Design Simulated Flight Conditions," *Journal of Turbomachinery* Vol. 128, No. 2, 2006, pp. 332-339.
doi: 10.1115/1.2098787

[8] Anderson, B. H., Miller, D. N., Addington, G. A., and Agrell, J. "Optimal Micro- Jet Flow Control for Compact Air Vehicle Inlets - NASA/TM-2004-212937." NASA Glenn Research Center, 2004.

[9] Gartner, J., and Amitay, M. "Flow Control in a Diffuser at Transonic Conditions," *AIAA Paper 2015-2484*, 2015.

[10] Rabe, A. "Effectiveness of a serpentine inlet duct flow control scheme at design and off- design simulated flight conditions." ProQuest Dissertations Publishing, 2003.

[11] Harrison, N., Anderson, J., Fleming, J., and Ng, W. "Active Flow Control of a Boundary Layer- Ingesting Serpentine Inlet Diffuser," *Journal of Aircraft* Vol. 50, No. 1, 2013, pp. 262-271.
doi: 10.2514/1.C031818

[12] Amitay, M., Pitt, D., and Glezer, A. "Separation control in duct flows," *Journal of Aircraft* Vol. 39, No. 4, 2002, pp. 616-620.
doi: 10.2514/2.2973

[13] Owens, L. R., Allan, B. G., and Gorton, S. A. "Boundary-Layer-Ingesting Inlet Flow Control," *Journal of Aircraft* Vol. 45, No. 4, 2008, pp. 1431-1440.
doi: 10.2514/1.36989

[14] Anderson, B. H., Mace, J. L., and Mani, M. "Active Fail- Safe Micro- Array Flow Control for Advanced Embedded Propulsion Systems - NASA/TM-2009-215596." Sponsoring Organization: NASA Glenn Research Center, 2009.

[15] Gissen, A. N., Vukasinovic, B., McMillan, M. L., and Glezer, A. "Distortion Management in a Boundary Layer Ingestion Inlet Diffuser Using Hybrid Flow Control," *Journal of Propulsion and Power* Vol. 30, No. 3, 2014, pp. 834-844.
doi: 10.2514/1.B34981

[16] Vaccaro, J. C., Elimelech, Y., Chen, Y., Sahni, O., Jansen, K. E., and Amitay, M. "Experimental and numerical investigation on steady blowing flow control within a compact inlet duct," *International Journal of Heat and Fluid Flow* Vol. 54, 2015, pp. 143-152.
doi: 10.1016/j.ijheatfluidflow.2015.05.011

[17] Garnier, E. "Flow Control by Pulsed Jet in a Curved S-Duct: A Spectral Analysis," *AIAA Journal* Vol. 53, No. 10, 2015, pp. 2813-2827.
doi: 10.2514/1.J053422

[18] Gil-Prieto, D., Zachos, P., MacManus, D. G., and Tanguy, G. "Convoluted Intake Distortion Measurements Using Stereo Particle Image Velocimetry," *AIAA Paper 2016-3560*, 2016.

[19] Gissen, A., Vukasinovic, B., and Glezer, A. "Dynamics of flow control in an emulated boundary layer- ingesting offset diffuser," *Exp Fluids* Vol. 55, No. 8, 2014, pp. 1-19.
doi: 10.1007/s00348-014-1794-5

[20] Burrows, T. J., Vukasinovic, B., and Glezer, A. "Fluidic Control of an Aggressive Offset Diffuser for a Supersonic Inlet," *AIAA Paper 2017-4304*, 2017.

[21] Towne, A., Schmidt, O. T., and Colonius, T. "Spectral proper orthogonal decomposition and its relationship to dynamic mode decomposition and resolvent analysis," *Journal of Fluid Mechanics* Vol. 825, 2017, pp. 1113-1152.